Supporting Information

Configuration-Dependent Hollow Heterostructures for Highly Efficient Photocatalytic Hydrogen Evolution

Yingqiang Li[#], Tao Zhang[#], Yifan Liu, Chao Liu, Jingwen Sun, Jianfei Che*, Pan Xiong*, Junwu Zhu

Key Laboratory for Soft Chemistry and Functional Materials of Ministry of Education, School of Chemistry and Chemical Engineering, Nanjing University of Science and Technology, Nanjing 210094, China

[#]These authors contributed equally.

*Corresponding author: xiaoche@mail.njust.edu.cn; pan.xiong@njust.edu.cn

Experimental

Chemicals

Sodium dodecyl sulfate ($C_{12}H_{25}SO_4Na$, SDS), potassium persulfate ($K_2S_2O_8$, KPS), styrene (C_8H_8), titanium dioxide (TiO_2), potassium carbonate (K_2CO_3), lithium carbonate (Li_2CO_3), tetrabutylammonium hydroxide ($C_{16}H_{37}NO$), poly dimethyl diallyl ammonium chloride (PDDA, $C_8H_{16}NCl)_n$), hydrochloric acid (HCl), and urea (CH_4N_2O) were procured from Aladdin Chemistry Co. Ltd. All chemicals were of analytical reagent grade and used without further purification.

Material characterization

Phase analysis of the samples was conducted using X-ray powder diffraction (XRD) on a Rigaku/MiniFlex600 instrument. Surface functional groups and chemical compositions of the products were characterized using Fourier transform infrared spectroscopy (FT-IR, NICOLETIS10) and X-ray photoelectron spectroscopy (XPS, ESCALAB250Xi). Morphological structures of the products were examined using a scanning electron microscope (SEM, Hitachi S4800) and a transmission electron microscope (TEM, JEOL JEM-2100) operated at 200 kV. Optical properties of the products were assessed using UV-vis diffuse-reflectance spectroscopy (UV-2550) and photoluminescence spectroscopy (PL, FLS1000) at room temperature. Reactive oxygen species (ROS), including electrons (e^-) and holes (h^+), in the composite solutions were identified and quantified using electron spin resonance spectroscopy (ESR, JESFA200).

Photocatalytic activity

Photocatalytic hydrogen production was quantified using an online system (LbSolar-3AG, PerfectLight, Beijing). 10 mg of the photocatalysts were dispersed in a 100 mL aqueous solution consisting of 90 mL water and 10 mL triethanolamine. Pt (serving as a co-catalyst) was subsequently deposited onto the material using the photo-deposition method. A solution of $H_2PtCl_6·6H_2O$ at 3 wt.% (relative to Pt) was introduced, degassed, and subsequently irradiated with a 300 W Xenon lamp (PLS-SXE 300C (BF), PerfectLight, Beijing) equipped with an AM-1.5 filter or an optical filter ($\lambda >$ 420 nm). Gas concentration was analyzed using an online gas chromatograph (GC D7900P, TCD

detector). Thermogravimetric analysis (TGA, TGA5500) was employed to assess sample weight loss, with a heating rate of 10 °C/min from room temperature to 800 °C.

Photoelectrochemical Experiments

Electrochemical impedance spectroscopy (EIS), transient photocurrent and Mott-Schottky plots were tested on CHI 660E (Chenhua Instrument, Shanghai, China) with a typical three-electrode cell employed 0.2 M Na_2SO_4 aqueous solution as the electrolyte. Ag/AgCl electrode and Pt wire were used as reference and counter electrodes, respectively. The working electrode was prepared as follows: 5 mg of photocatalyst was dispersed into mixed solution including ethanol (250 µL), ethylene glycol (250 µL), and Nafion (40 µL) and then sonicated for 20 min. Then, the above solution (80 µL) was dropped onto a precleaned fluorine tin oxide (FTO) glass with an exposed area of 1 cm^2. A 300 W Xenon (Xe) lamp equipped with a 420 nm cutoff filter served as the visible light source. The photocurrent responses of the photocatalysts to light switching on and off were measured with 1.2 V bias voltage. EIS spectra were recorded in the range from 0.01 to 10^5 Hz at an ac voltage of 10 mV. Mott-Schottky plots of material were then tested at 500 Hz frequencies by using the Impedance-Potential mode.

Theoretical calculation

The density functional theory (DFT) calculations were performed by Vienna Ab-initio simulation package (VASP). The exchange and correlation interactions were calculated by using generalized-gradient approximations (GGA) and Perdew-Burke-Ernzerhof (PBE) functional. For the calculation of electronic properties, the more accurate hybrid functional Heyd-Scuseria-Ernzerhof (HSE06) was also used to correct the results. The energy cutoff of electron wave functions was set to 600 eV and the k-point meshes of $6 \times 4 \times 1$ are used. The calculated lattice parameters of anatase TiO_2 are a = b = 3.784 Å and c = 9.515 Å. The optimized lattice parameters of monolayer g-C_3N_4 are a = b = 4.785 Å. All the atomic positions are fully relaxed until the force is smaller than 0.01 eV/Å and the energy tolerances less than 1.0×10^{-6} eV per atom.

a

1 µm

b

500 nm

c

500 nm

d

500 nm
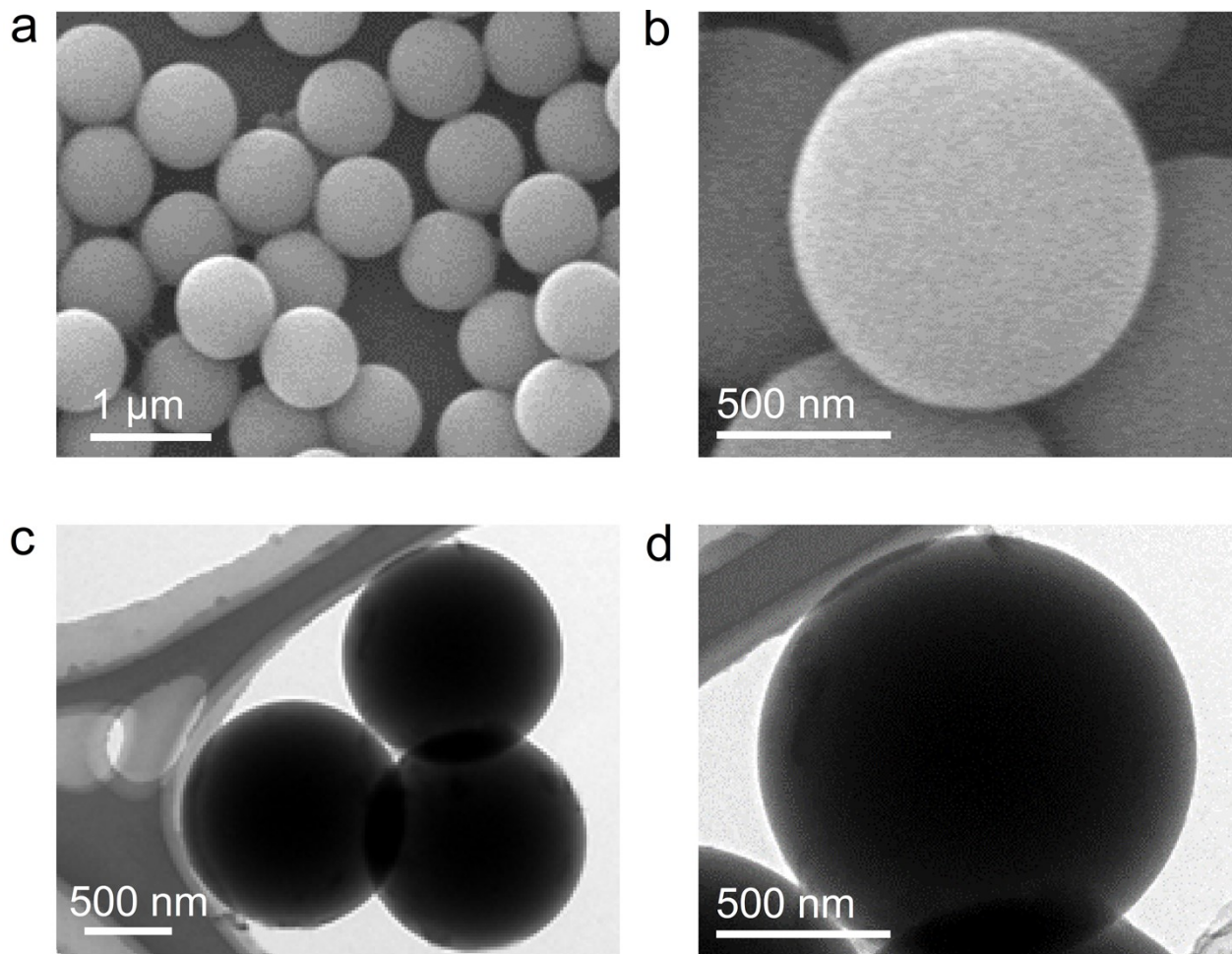
Figure S1 (a-b) SEM and (c-d) TEM images of PS microsphere modified with PDDA.

4
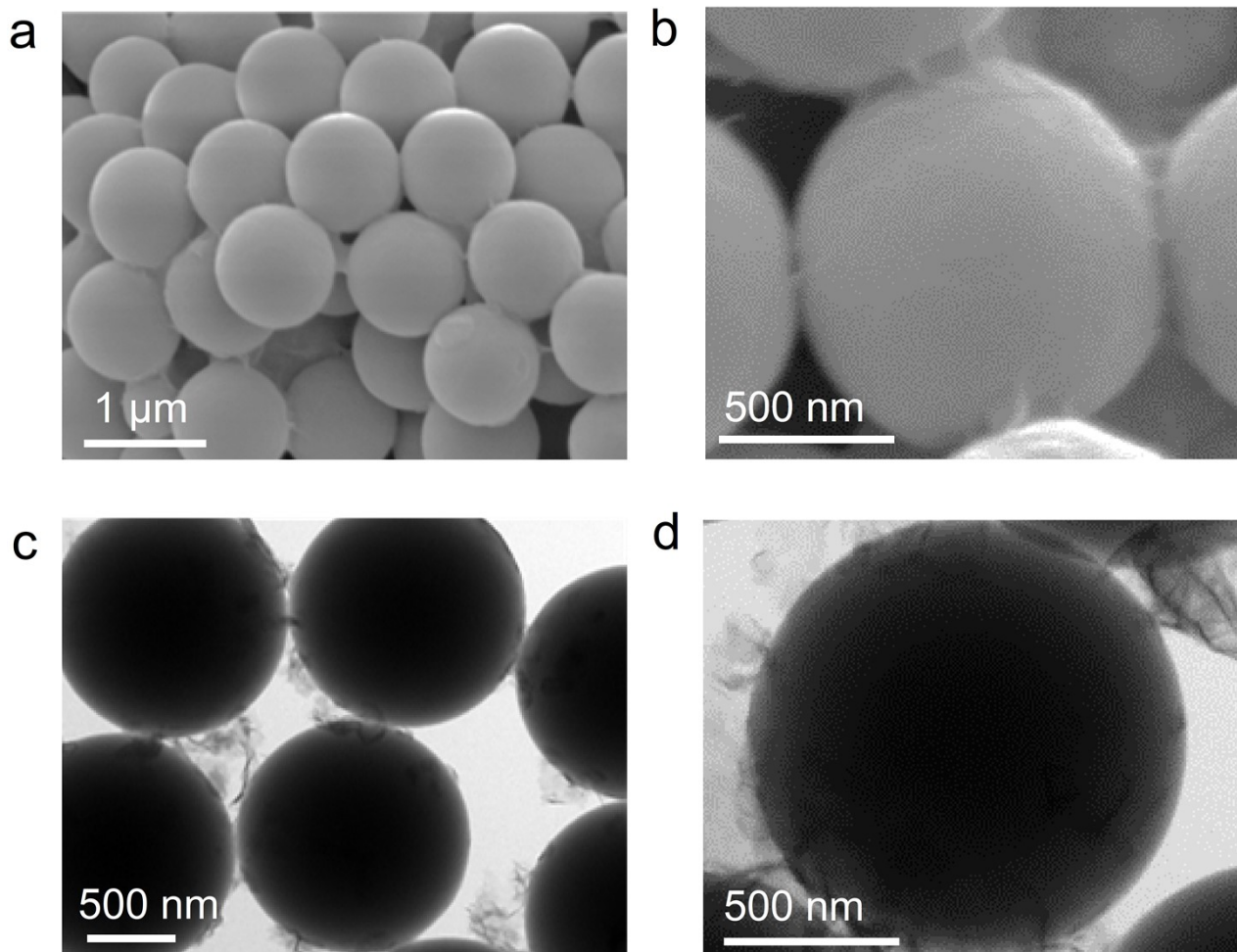
Figure S2 (a-b) SEM and (c-d) TEM images of $Ti_{0.87}O_2$/PS sphere.
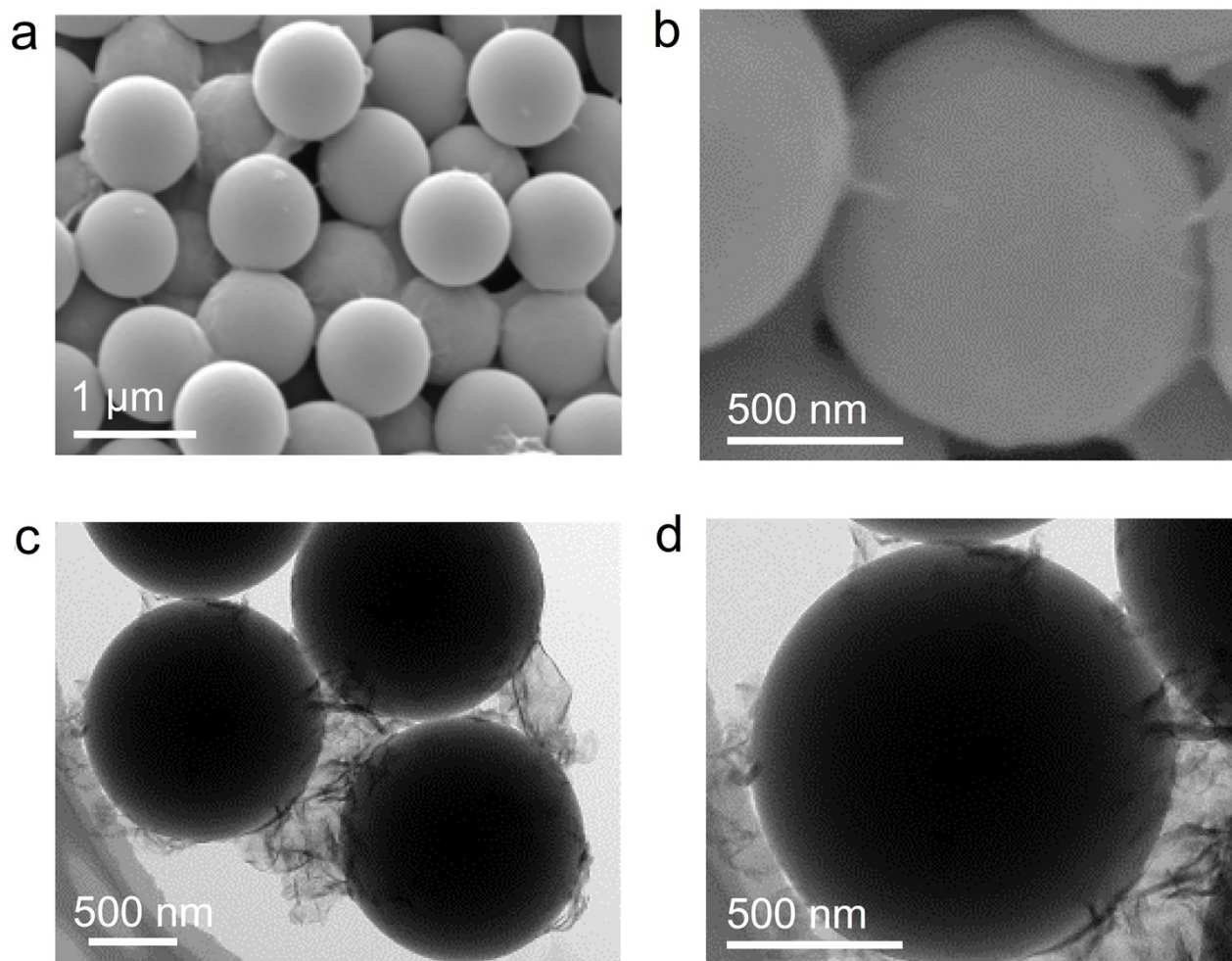
Figure S3 (a-b) SEM and (c-d) TEM images of g-C$_3$N$_4$/Ti$_{0.87}$O$_2$/PS sphere.
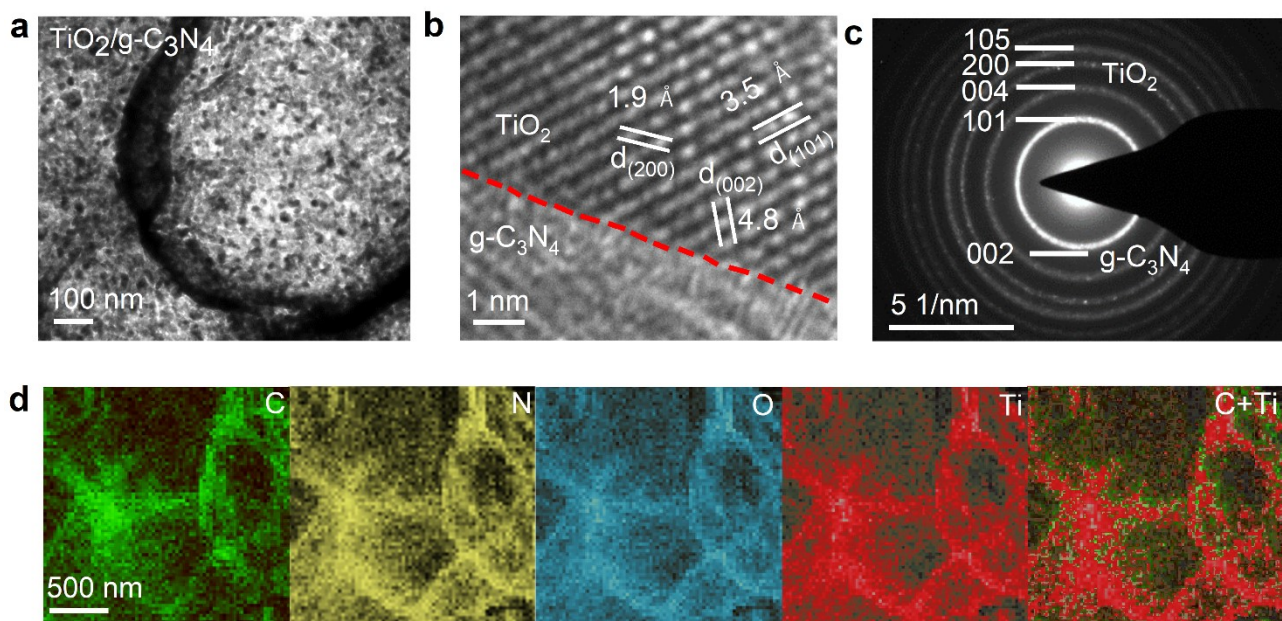
Figure S4 (a) TEM micrographs, (b) high-resolution TEM image, (c) SAED pattern and (d) elemental distribution mapping of A-TiO$_2$/g-C$_3$N$_4$.
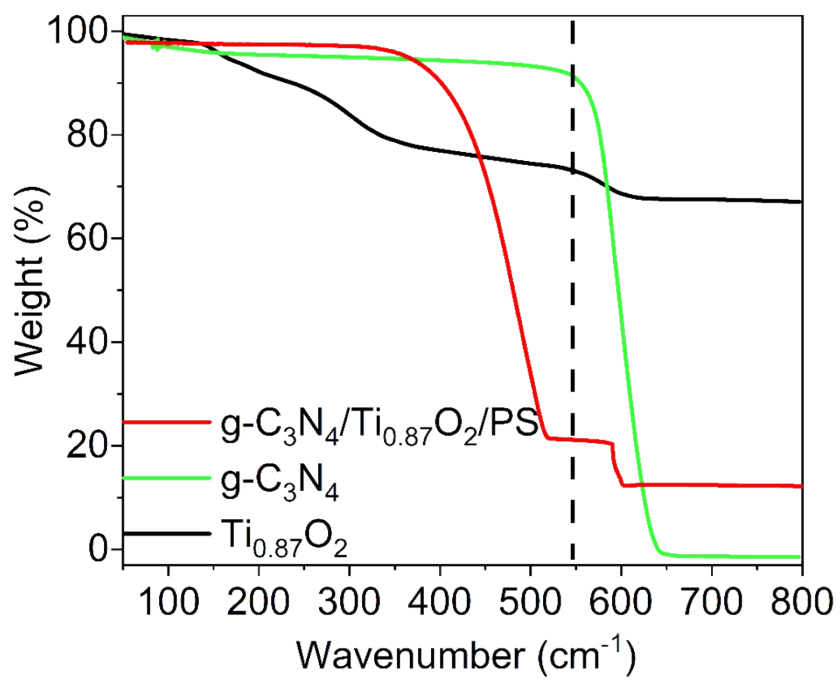
Figure S5 TGA curve of g-C$_3$N$_4$/Ti$_{0.87}$O$_2$/PS, g-C$_3$N$_4$ and Ti$_{0.87}$O$_2$.
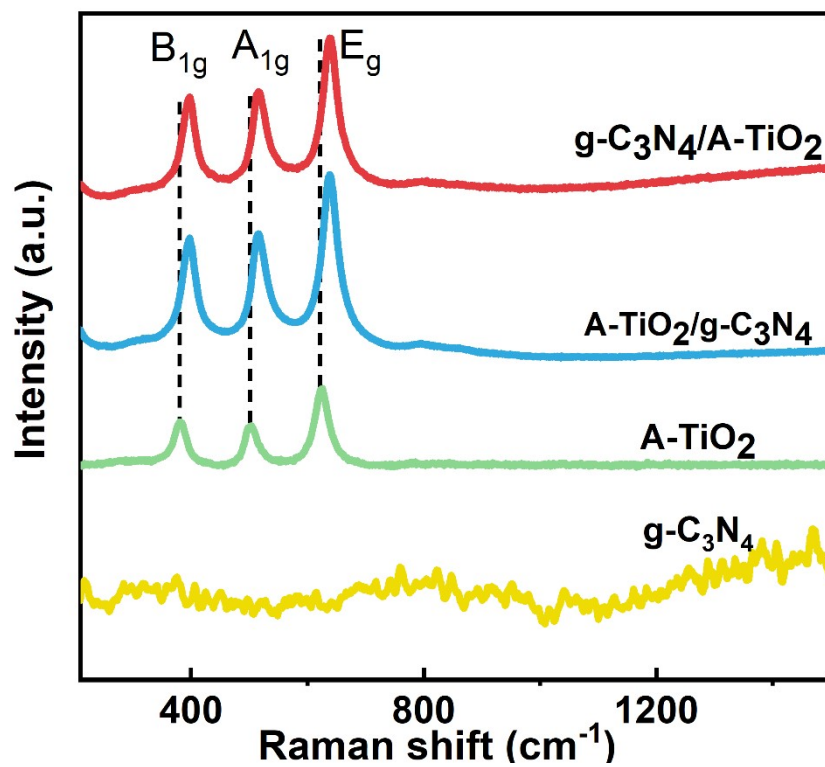
Figure S6 The Raman spectra of g-C_3N_4/A-TiO_2, A-TiO_2/g-C_3N_4, A-TiO_2 and g-C_3N_4.
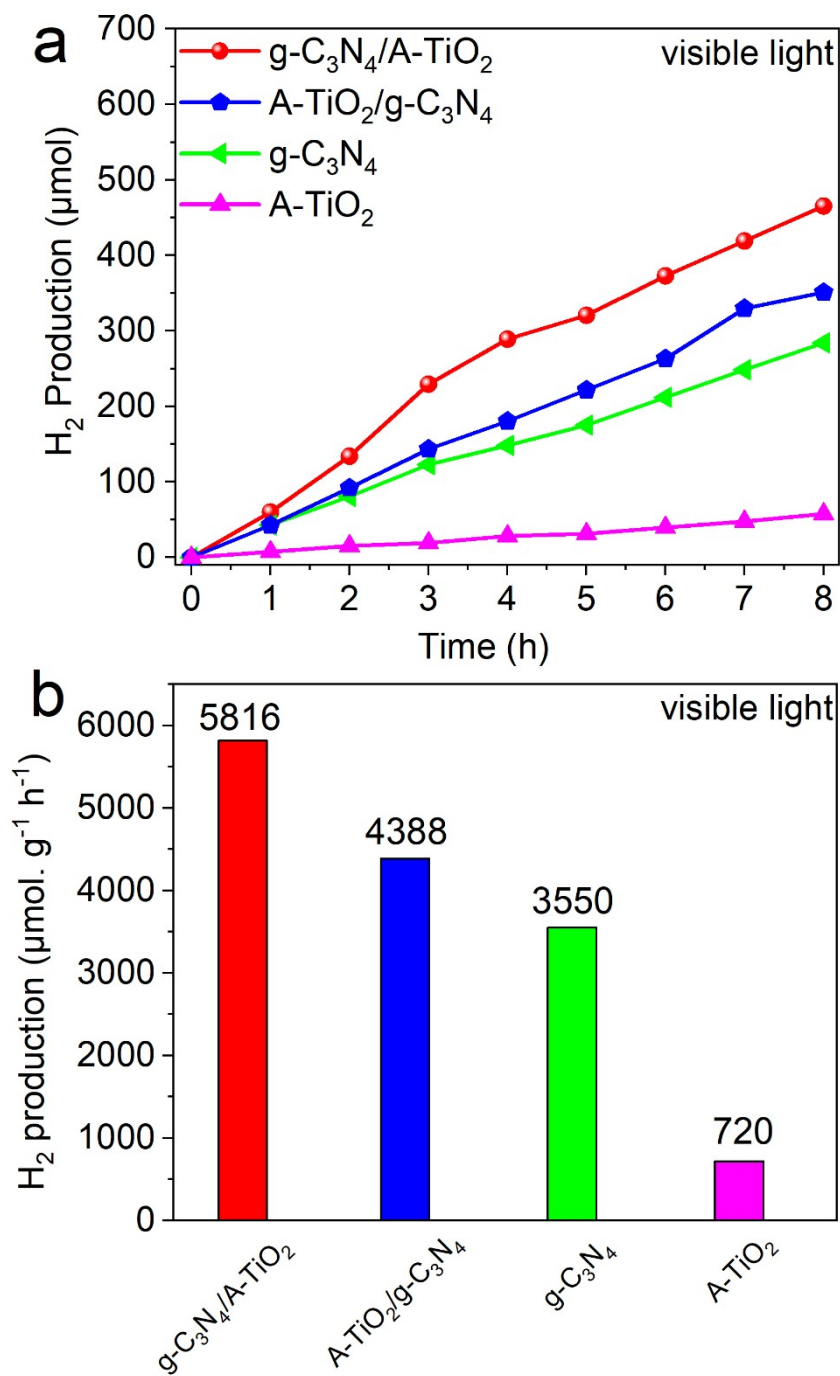
Figure S7 (a) Time course of hydrogen evolution and (b) comparison of hydrogen evolution rates for g-C_3N_4/A-TiO_2, A-TiO_2/g-C_3N_4, A-TiO_2 and g-C_3N_4 under visible light.
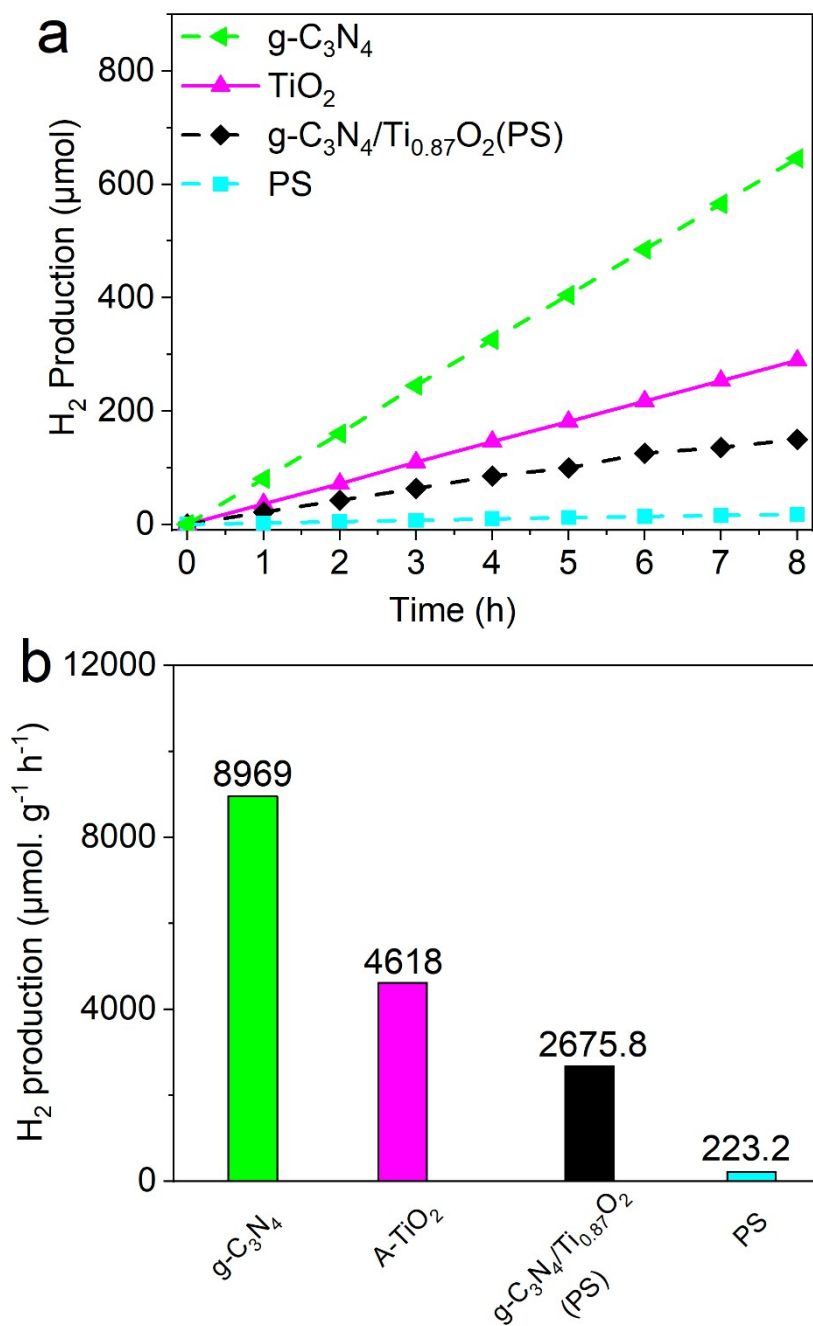
Figure S8 (a) Time course of hydrogen evolution and (b) comparison of hydrogen evolution rates for A-TiO$_2$, g-C$_3$N$_4$, g-C$_3$N$_4$/Ti$_{0.87}$O$_2$/PS and PS materials.
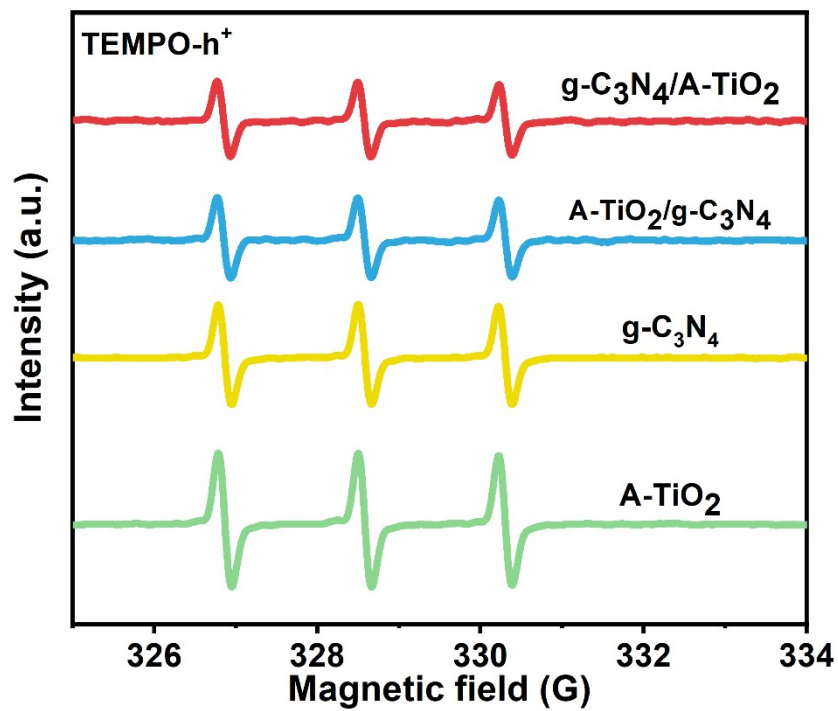
Figure S9 ESR spectra of e⁻ of g-C$_3$N$_4$/A-TiO$_2$, A-TiO$_2$/g-C$_3$N$_4$, g-C$_3$N$_4$ and TiO$_2$ when exposed to solar light for a duration of 9 minutes.
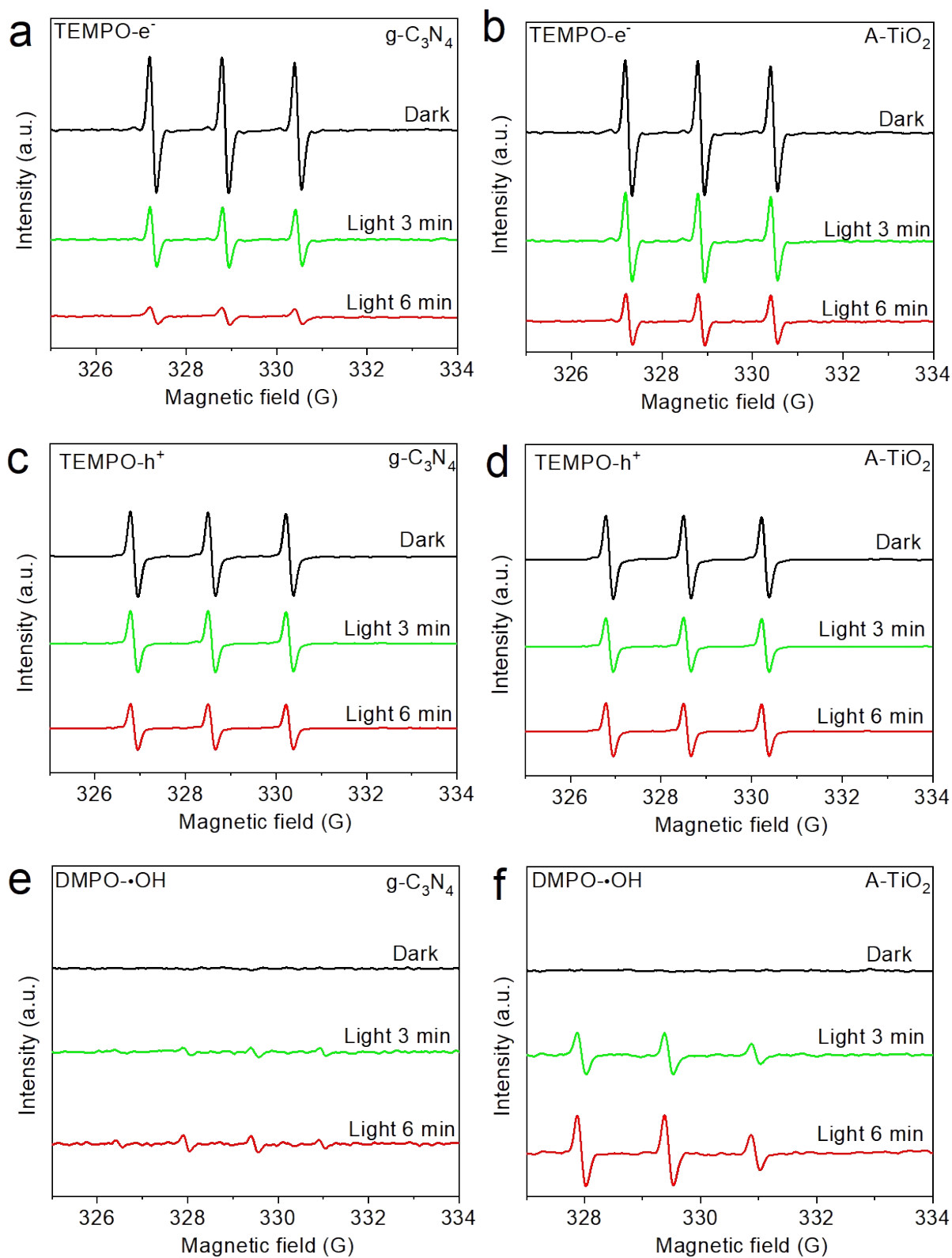
Figure S10 ESR spectra of (a) e$^-$ of g-C$_3$N$_4$, (b) e$^-$ of TiO$_2$, (c) h$^+$ of g-C$_3$N$_4$, (d) h$^+$ of TiO$_2$, (e) •OH of g-C$_3$N$_4$ and (f) •OH of TiO$_2$ under solar light irradiation for various times.
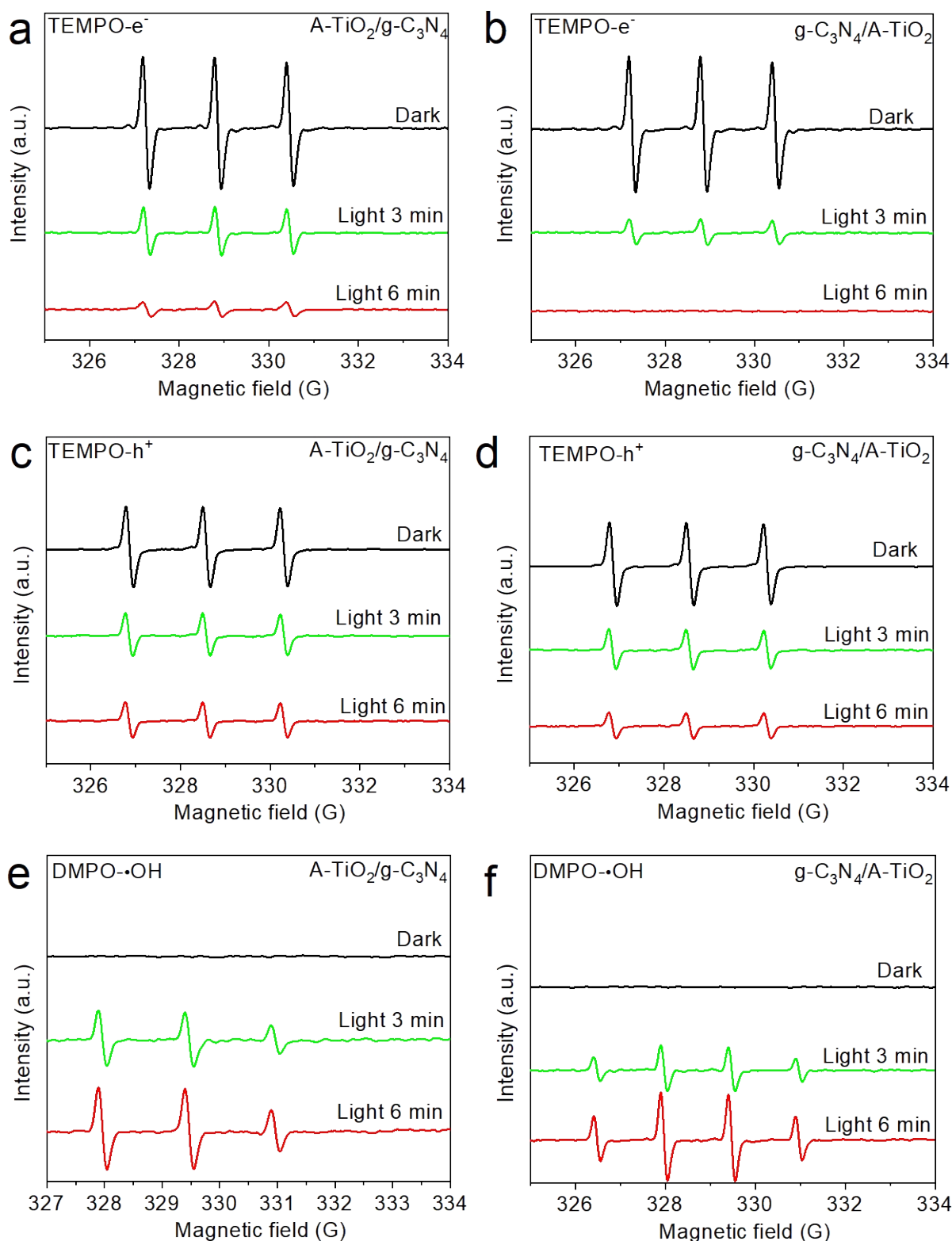
Figure S11 ESR spectra of (a) e^- of A-TiO$_2$/g-C$_3$N$_4$, (b) e^- of g-C$_3$N$_4$/ A-TiO$_2$, (c) h^+ of A-TiO$_2$/g-C$_3$N$_4$, (d) h^+ of g-C$_3$N$_4$/ A-TiO$_2$, (e) •OH of A-TiO$_2$/g-C$_3$N$_4$ and (f) •OH of g-C$_3$N$_4$/ A-TiO$_2$ under solar light irradiation for various times.
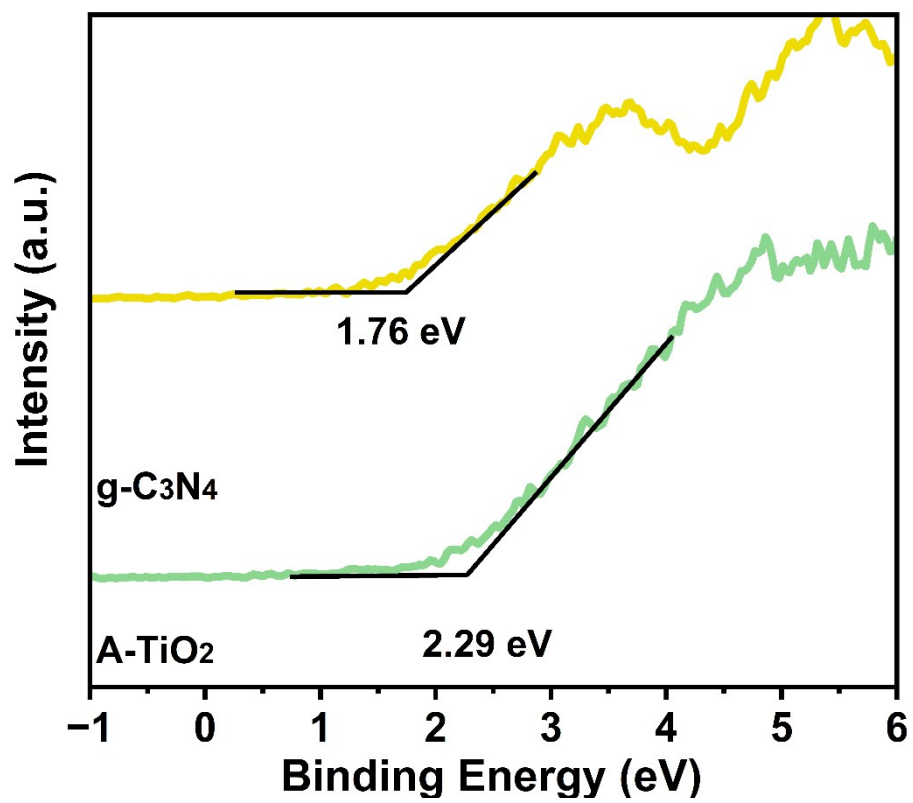
Figure S12 VB-XPS survey of g-C$_3$N$_4$ and TiO$_2$.
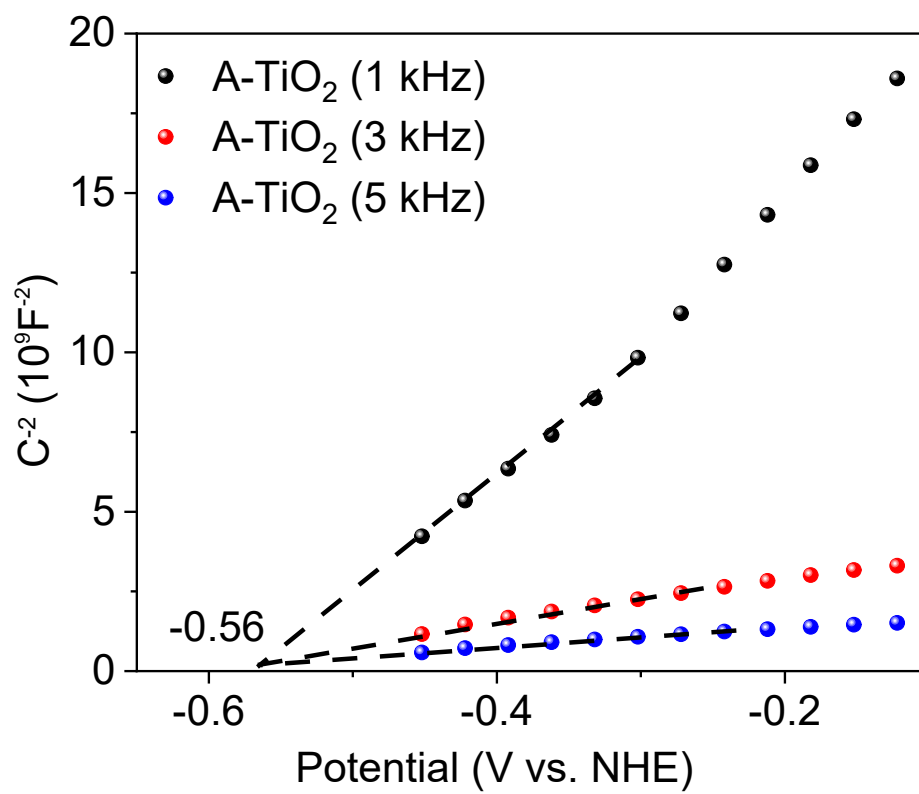
Figure S13 Mott-Schottky plots at different frequencies of A-TiO$_2$.
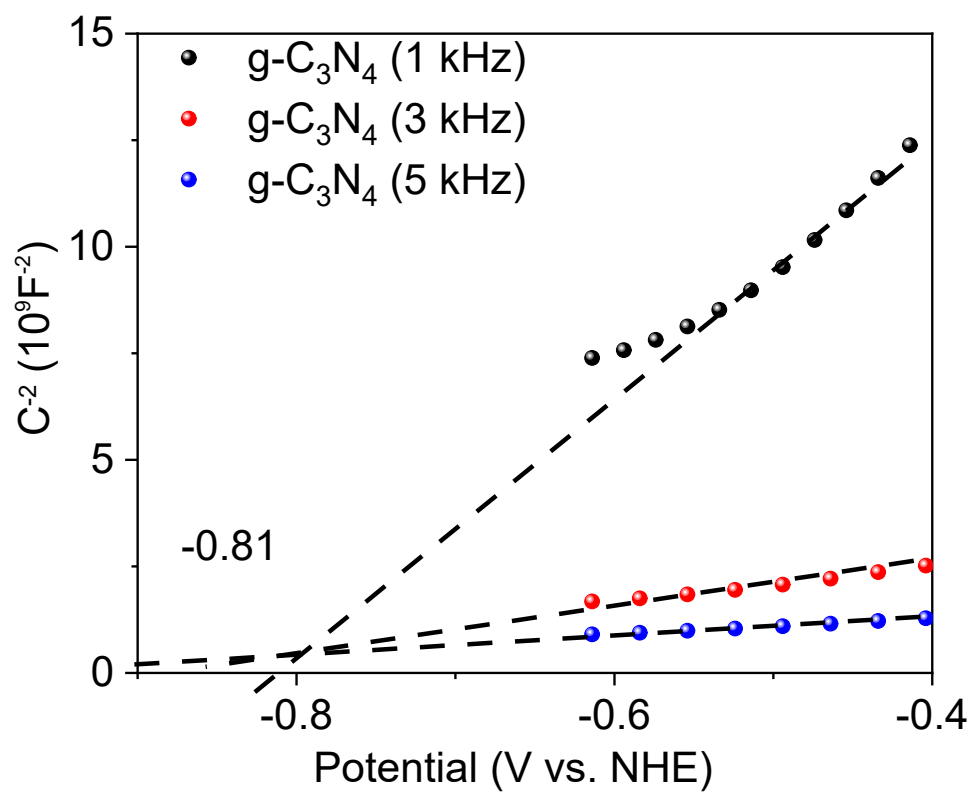
Figure S14 Mott-Schottky plots at different frequencies of g-C_3N_4.
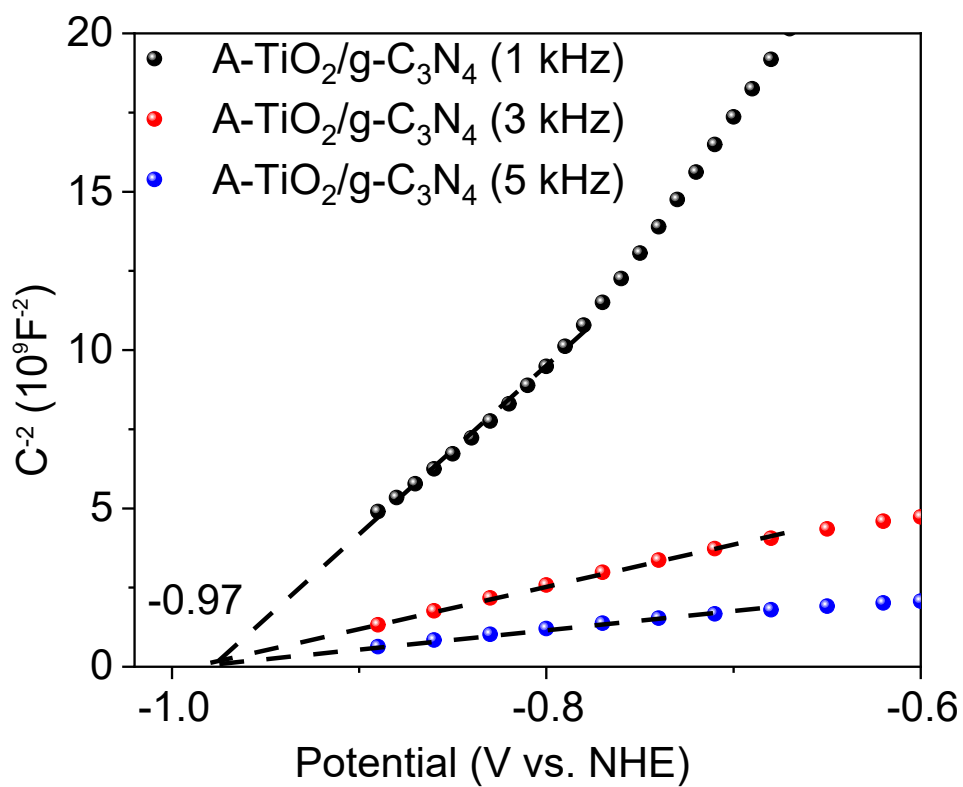
Figure S15 Mott-Schottky plots at different frequencies of A-TiO$_2$/g-C$_3$N$_4$.
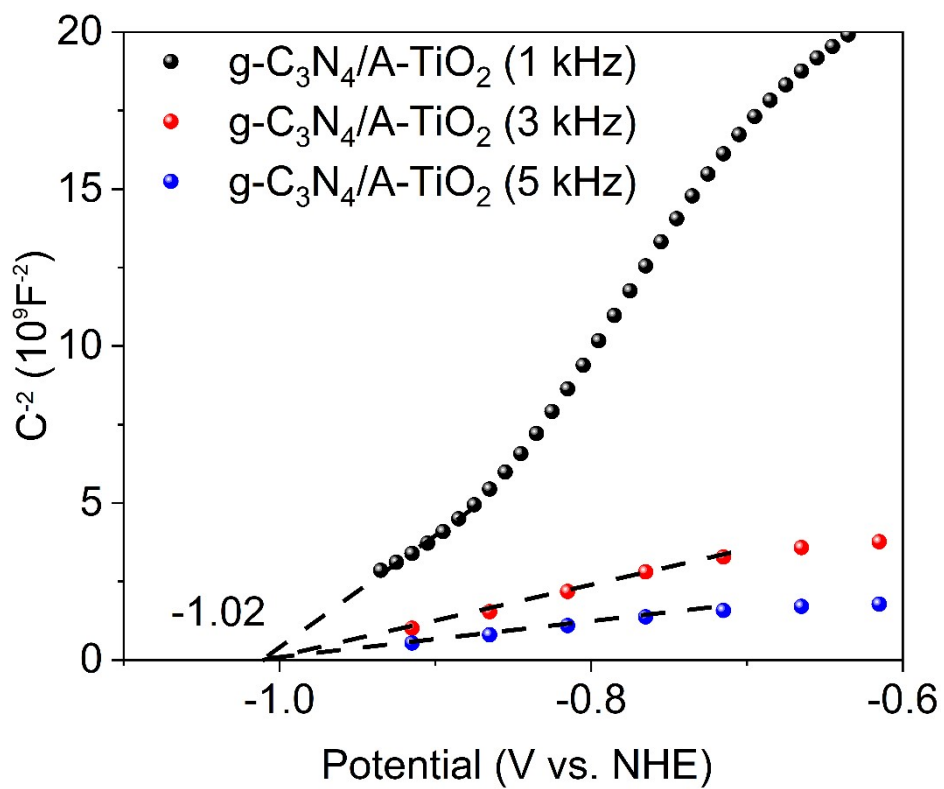
Figure S16 Mott-Schottky plots at different frequencies of g-C$_3$N$_4$/A-TiO$_2$.
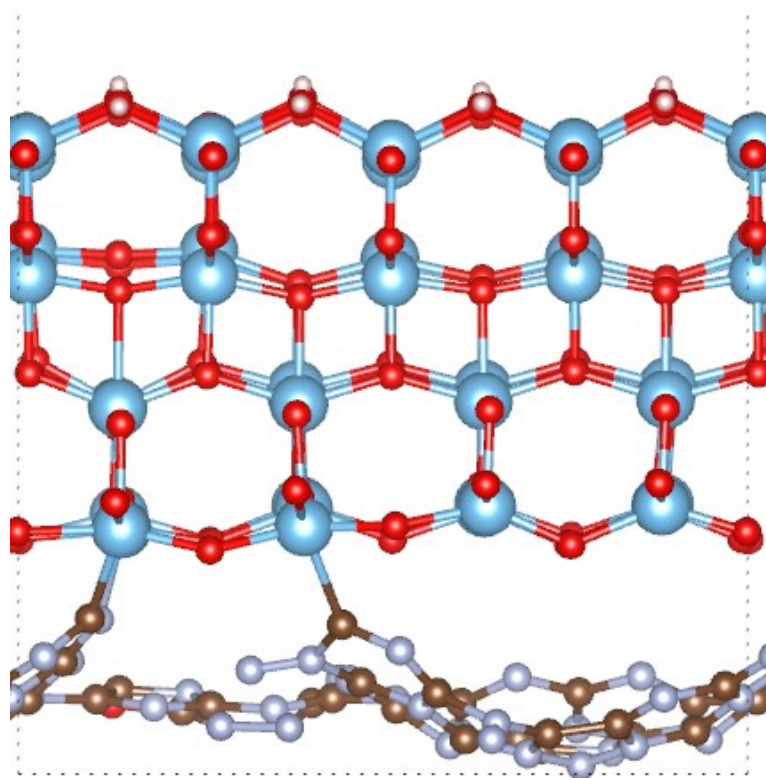
Figure S17 The optimized structures of A-TiO$_2$/g-C$_3$N$_4$ heterostructure.
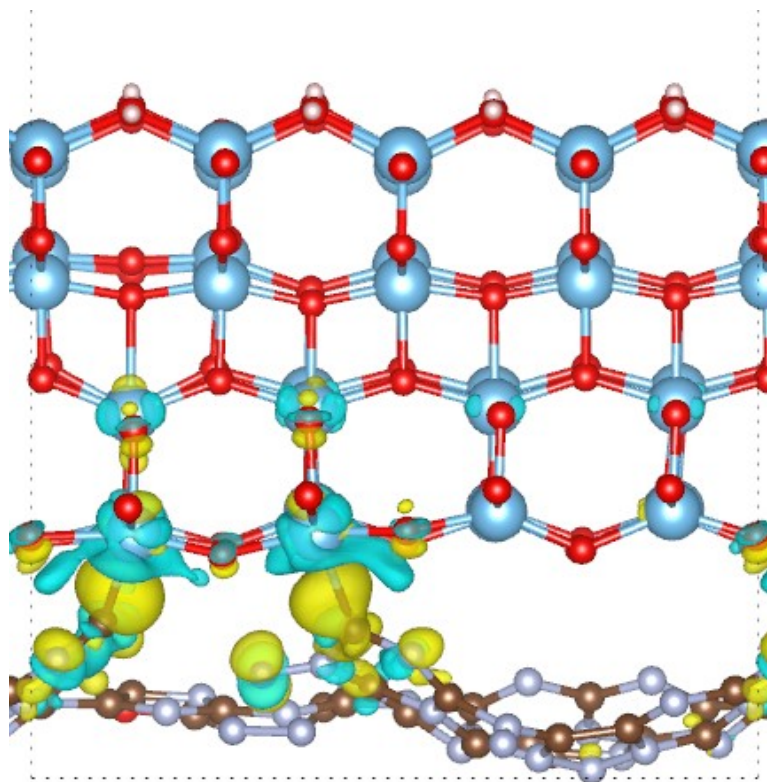
Figure S18 Charge density difference of A-TiO_2/g-C_3N_4 heterostructure. The yellow and blue in the figure represent the accumulation and loss of electrons.
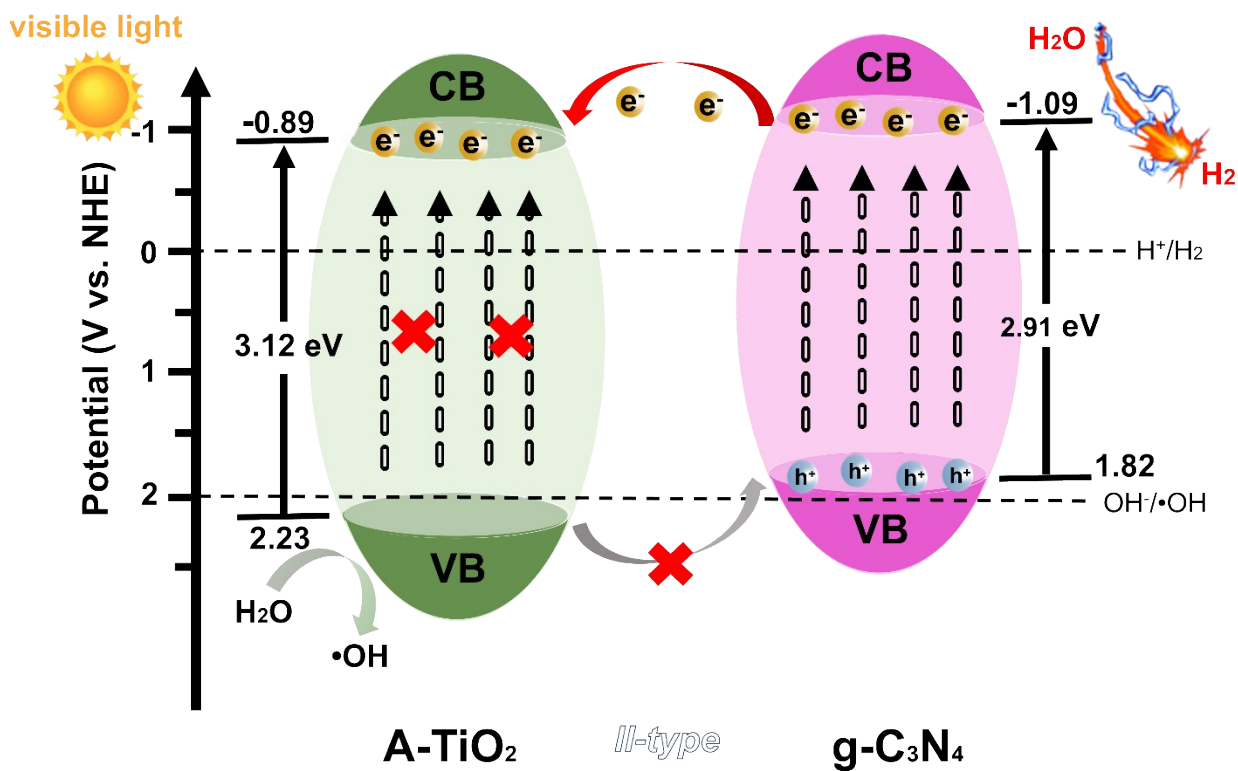
Figure S19 An illustration of photocatalytic mechanism of g-C$_3$N$_4$/TiO$_2$ under visible light.

Table S1 Comparison of Zeta potential of samples in the pure water.

Sample	Zeta Potential (mV)	Standard Deviation (mV)
g-C_3N_4	−12.8	5.72
$Ti_{0.87}O_2$	−35.5	4.54
PDDA/PS	+22.8	3.82